ELSEVIER

Nuclear Physics A 696 (2001) 293–316

NUCLEAR PHYSICS A

www.elsevier.com/locate/npe

Giant resonance spectroscopy of ^{40}Ca with the (e, e′x) reaction (II): Multipole decomposition of 4π-integrated spectra and angular correlations ☆

H. Diesener [a,1], U. Helm [a,2], V. Huck [a,3], P. von Neumann-Cosel [a,*], C. Rangacharyulu [a,4], A. Richter [a], G. Schrieder [a], A. Stascheck [a], S. Strauch [a,5], J. Ryckebusch [b], J. Carter [c]

[a] *Institut für Kernphysik, Technische Universität Darmstadt, D-64289 Darmstadt, Germany*
[b] *Department for Subatomic and Radiation Physics, University of Gent, Proeftuinstraat 86, B-9000 Gent, Belgium*
[c] *School of Physics, University of the Witwatersrand, PO Wits, Johannesburg, 2050 South Africa*

Received 21 August 2000; revised 7 May 2001; accepted 14 June 2001

Abstract

The present article is the second out of three on a study of the ^{40}Ca(e, e′x) reaction discussing the multipole decomposition of the measured cross sections and the analysis of angular correlations. The decomposition of the strongly overlapping E0, E1 and E2 giant resonance strengths using the (e, e′x; $x = \mathrm{p}, \alpha$) reaction in ^{40}Ca is discussed for excitation energies between 10 and about 21 MeV. Two extraction methods are presented based on the variation of the form factors for the different multipoles. The resulting B(E1) strength distribution is in good agreement with (γ, x) photoabsorption data. The summed B(E2) and B(E0) strength is highly fragmented and spread out over the energy region investigated. Microscopic continuum RPA calculations including the coupling of the basic particle–hole states to the low-lying surface vibrations are capable of reproducing the strength distributions quite accurately. Exhaustion of the energy-weighted sum rules (EWSR) for the various decay channels is presented.

A complete decomposition of E0, E1 and E2 contributions in ^{40}Ca is possible for (e, e′α) angular correlations populating the ^{36}Ar ground state. Contrary to expectations, the form factors

☆ Work supported by the DFG under contract FOR 272/2-1 and through SFB 201.

* Corresponding author.
E-mail address: vnc@ikp.tu-darmstadt.de (P. von Neumann-Cosel).
[1] Present address: EDS, D-63037 Offenbach, Germany.
[2] Deceased.
[3] Present address: ABB, D-68185 Mannheim, Germany
[4] Visitor from the Department of Physics, University of Saskatchewan, S7N5E2 Saskatoon, Canada.
[5] Present address: Department of Physics and Astronomy, Rutgers University, Piscataway, NJ 08854, USA.

0375-9474/01/$ – see front matter
PII: S0375-9474(01)01209-X

of isoscalar E0 and E2 strengths in the ^{40}Ca(e, e′α_0) reaction exhibit increasing differences towards smaller momentum transfers. Angular correlations for proton decay into low-lying states of ^{39}K are compared to a self-consistent continuum RPA calculation which allows a systematic description of the strong variations observed as a function of ^{40}Ca excitation energy and momentum transfer. The success implies that direct knock-out models of the ^{40}Ca(e, e′p) reaction are too simple. Furthermore, the shapes of the angular correlations seem to be determined largely by the final-state interaction, in particular by charge exchange reactions in the nuclear medium.

PACS: 25.30.Fj; 27.40.+z; 21.10.Re; 21.60.Jz
Keywords: NUCLEAR REACTION ^{40}Ca(e, e′p), (e, e′α), $E_0 = 78, 183.5$ MeV; measured angular correlations of p, α decay into low-lying states of ^{39}K and ^{36}Ar; ^{40}Ca deduced E0, E1, E2 strength distributions. Continuum RPA calculations

1. Introduction

The basic quantities characterizing giant resonances are their total strengths, usually expressed in terms of model-independent energy-weighted sum rules (EWSR), and their distributions in energy. Because of the large energy spreading of the resonances over regions of several MeV, one is often confronted with strongly overlapping contributions from different multipoles and isospins.

The subject of the present investigations, the doubly magic nucleus ^{40}Ca, provides a particularly good example. The isovector giant dipole (GDR) as well as the isoscalar giant quadrupole (GQR) and monopole (GMR) resonances are spread out over an excitation energy interval of about 10–25 MeV and are mingled strongly. Although extensive experimental work has been devoted to the study of ^{40}Ca with its doubly-magic shell structure making it a favorite testing ground of theoretical investigations, there remain a number of unsolved issues. The main features of the GDR have been established reasonably well by photoabsorption experiments [1,2], revealing a low-energy tail extending down to about 10 MeV excitation with considerable structure. The GQR was located in various experiments to be around 18 MeV excitation. However, a ^{40}Ca($\alpha, \alpha' x$) study [3] showed the existence of appreciable E2 strength at low excitation energies with a concentration at $E_x \approx 12$–14 MeV and a remarkably large exhaustion of the isoscalar E2 EWSR of about 60% below 16 MeV. Such a result was in clear contradiction to RPA calculations [4–6] which predicted the strength to be centered at 18 MeV excitation. In addition, the GMR was shown experimentally to be fragmented strongly over a very large energy interval [7] with a considerable part of the strength at excitation energies below 15 MeV. The nucleus ^{40}Ca also serves as a testing ground of giant resonance fine structure, a phenomenon which appears in nuclei as heavy as ^{208}Pb [8]. This fine structure constitutes a challenge to microscopic interpretations of giant resonances and can be accounted for only in the most advanced theories [9,10].

Electron-scattering coincidence experiments offer a particularly powerful tool for multipole decomposition. The electromagnetic interaction in electron scattering is weak and can be described well in perturbation theory [11], unlike hadronic reactions which

are hampered by a limited knowledge of the nucleon–nucleon interaction. The coincidence condition with particle emission out of the continuum effectively removes the radiative tails due to elastic scattering and inelastic scattering to bound states, thus permitting essentially background-free measurements.

Two methods of multipole strength decomposition are discussed in the present paper. With some reasonable assumptions it is possible to reconstruct the total excitation cross sections by an integration over the solid angle of the emitted particle (4π integration). The multipoles can be separated by variation of the momentum transfer. Two different approaches will be discussed, a so-called 'model-independent' method [12,13] and a decomposition based on microscopic form factors [14–16]. A successful application of the former method to our ^{40}Ca data was reported in [17]. However, E2 and E0 contributions cannot be distinguished with these methods because of the similarity of their form factor dependence.

Alternatively, in the framework of the 'static limit of resonance' approach (SLRA) of [18], all multipole contributions can be extracted from angular correlation functions (ACFs) for decay to specific final states. Again, there are limitations to the number of simultaneously contributing multipoles which can be resolved. The simplest case, which can be treated analytically [19], are angular correlations of the type $0^+ \rightarrow \lambda^\pi \rightarrow 0^+$. This case is realized for (e, e′α_0) reactions on even–even target nuclei and has been utilized to resolve discrepancies of the multipole strengths deduced from different hadron-induced reactions in ^{12}C and ^{16}O [20,21]. Another application on ^{26}Mg is reported in [22].

The ^{40}Ca(e, e′α_0) channel populating the ground state (g.s.) of ^{36}Ar is of special interest, because it allows a detailed comparison [23] with extensive ^{40}Ca($\alpha, \alpha'\alpha_0$) [3,24] and (p, p′α_0) [25–27] studies. A consistent picture of the fine structure of the GMR and GQR at low excitation energies is achieved. However, a factor of two larger EWSR value is obtained in the α-scattering experiment which yet lacks explanation. Recently, it was demonstrated for the example of the ^{40}Ca(e, e′α_1) data that the multipole unfolding method can be extended with a few well-founded assumptions to angular correlations for the population of a $J^\pi = 2^+$ final state [28]. The present paper will only briefly touch upon a few aspects of these results which have not been covered in [23,28].

For ACFs of the type (e, e′N), where N denotes a nucleon, one must additionally take into account the incoherent summation of the coupling to different spin channels which further complicates the analysis. If one multipolarity dominates, useful results might still be obtained [29]. Data on the ^{40}Ca(e, e′p$_0$) [30] and (e, e′n$_0$) [31] reactions exist for a single momentum transfer favoring E1 excitations. These have been analysed with an emphasis on the interference of longitudinal and transverse contributions. However, when several multipoles contribute with comparable magnitude to the cross sections (as is the case for ^{40}Ca in the present kinematic conditions) a model-independent decomposition is no longer possible. Instead, the ^{40}Ca (e, e′p) angular correlations are tested against a continuum-RPA approach [32] which has been used successfully to describe the interference region between the resonance and quasielastic domains [33].

The ^{40}Ca(e, e′x; $x = \mathrm{p}, \alpha$) experiment and the data reduction have been described in the preceding paper (hereafter called I). Section 2 is devoted to a multipole analysis of

the measured spectra, while Section 3 discusses the ^{40}Ca(e, e′α) angular correlations. The analysis of ^{40}Ca(e, e′p) angular correlations leading to low-lying states in ^{39}K are presented in Section 4. Concluding remarks are given in Section 5.

2. Multipole analysis of the 4π-integrated spectra

2.1. Methods

The extraction of 4π integrated $(e, e'x)$ spectra representing the total excitation in ^{40}Ca correlated with charged particle decay is described in part I. Two of the main assumptions discussed there are essential also for the analysis described in the following: the kinematics of the experiment are such that transverse and longitudinal-transverse parts of the coincident cross sections are negligible, and only multipolarities $\lambda \leqslant 2$ contribute. Then the 4π integrated cross section can be written as a function of excitation energy E_x and momentum transfer q as

$$\frac{d^2\sigma_i}{d\Omega_e\, dE_{x,j}} = \left(\frac{d\sigma}{d\Omega}\right)_{Mott} \sum_{\lambda=0}^{2} a_{E\lambda}(E_{x,j}) \left|F_{E\lambda}(q_i, E_{x,j})\right|^2. \tag{1}$$

Here, $a_{E\lambda}$ are the amplitudes of the different multipolarities, varying with q, and $F_{E\lambda}$ are the form factors. The indices j represent different excitation energy bins. Equation (1) can be written separately for each momentum transfer i measured. Since the momentum transfer dependence of E0 and E2 excitations is expected to be very similar (see, however, Section 3), only their sum can be determined and Eq. (1) can be rewritten as

$$\frac{\sigma_{exp}}{\sigma_{Mott}}(q_i, E_{x,j}) = a_{E1}(E_{x,j}) \left|F_{E1}(q_i)\right|^2 + a_{E2/E0}(E_{x,j}) \left|F_{E2/E0}(q_i)\right|^2, \tag{2}$$

where the further assumption of excitation energy independence of the form factors is made [12,13]. Here, σ_{exp} and σ_{Mott} are used as abbreviations for the respective differential cross sections introduced in Eq. (1). Equation (2) reduces to a series of $i \times j$ linear equations with the coefficients a_j and form factors F_i as variables. If the number of momentum transfers measured is larger than the number of multipoles, the equation system is overdetermined and can be solved by a least-squares fit to the data.

An alternative approach is based on the use of microscopically generated form factors. The E1 versus E2(E0) decomposition is then obtained by a least-squares fit to the experimental form factors, either for the total charged particle decay or for partial decay channels. The form factors are plotted as a function of the effective momentum transfer

$$q_{eff} = q\left(1 + \frac{3}{2}\frac{Ze^2}{\hbar c E_0 R_e}\right), \tag{3}$$

with R_e giving the equivalent radius. This correction accounts in an approximate way for the distortion of the electron wave function in the Coulomb field of the nucleus.

For both methods theoretical form factors are needed to extrapolate the deduced cross sections to the photon point $k = E_x/\hbar c$ and to make the conversion to reduced transition strengths

$$B(\mathrm{E}\lambda) = \frac{[(2\lambda+1)!!]^2}{k^{2\lambda}} \frac{Z^2}{4\pi} \left| F_{\mathrm{E}\lambda}(q=k) \right|^2. \quad (4)$$

Theoretical results from two different sources were considered for the analysis. Electric excitations for all multipolarities $\lambda \leqslant 4$ were calculated in RPA [34] using the separable MSI interaction [35]. For the E0 and E2 multipolarities a single collective transition around 18 MeV excitation is predicted representing the GMR and GQR, respectively. From the several E1 excitations obtained, the shape of the by far strongest transition was taken to represent the GDR. More refined calculations are provided by Kamerdzhiev et al. [36, 37] including 1p–1h $\otimes$ phonon configurations and coupling to the continuum. Here, the interaction is of the Migdal type [38]. However, differences between the form factors resulting from the two approaches are small.

It should be noted that the results of [36] allowed a test of the assumption of energy independence, at least for the isoscalar E2 form factor where separate transition densities for the energy regions $E_x = 10$–16 MeV and 16–23 MeV were available [39]. Form factors obtained from these transition densities as well as transition strengths at the photon point from the two different calculations varied less than 10%. Thus, in the following results based on E2 form factors of [36,37] are discussed.

2.2. Model-independent analysis

A detailed analysis revealed that the model-independent method does not provide unique solutions without additional constraints. Therefore, data for the (γ, x) reaction (where x represents charged particle decay) were included in the fit. The (γ, x) cross sections could be deduced from the difference between a total photoabsorption experiment [1] and a (γ, n) measurement [2].

The results of the above procedure are shown in Fig. 1 for the data taken at MAMI [40]. The upper row gives the experimental spectra. Below, the resulting E1 and E2(E0) cross sections are displayed. The lowest row gives the residue of the least-squares fit. It is generally small except for two distinct peaks around 12 MeV which are most pronounced at the highest momentum transfer. Probably, these can be attributed to E3 strength. Considerable fine structure is visible for both, E1 and E2(E0) cross sections, especially below 15 MeV excitation. The variation of the ratio of E1 and E2(E0) cross-section parts reflects the momentum transfer dependence.

It is instructive to compare these results to an analysis of inclusive $(\mathrm{e}, \mathrm{e}')$ scattering on ^{40}Ca under nearly identical kinematical conditions [41] plotted in Fig. 2. The decomposition in the latter experiment was based on calculated form factors. While the experimental cross sections agree favorably, the analysis of [41] clearly underestimates the low-energy part of the E1 strength and also the E2 contribution underneath the main peak of the GDR.

Cross sections can be converted to reduced transitions strengths as described in Section 2.1 The resulting $B(\mathrm{E1})$ and $B(\mathrm{E2}+\mathrm{E0})$ strength distributions in ^{40}Ca up to an excitation energy of 20.5 MeV are depicted in Fig. 3. Here, the results for E1 are compared to the strength distribution extracted from photoabsorption data [1]. The full

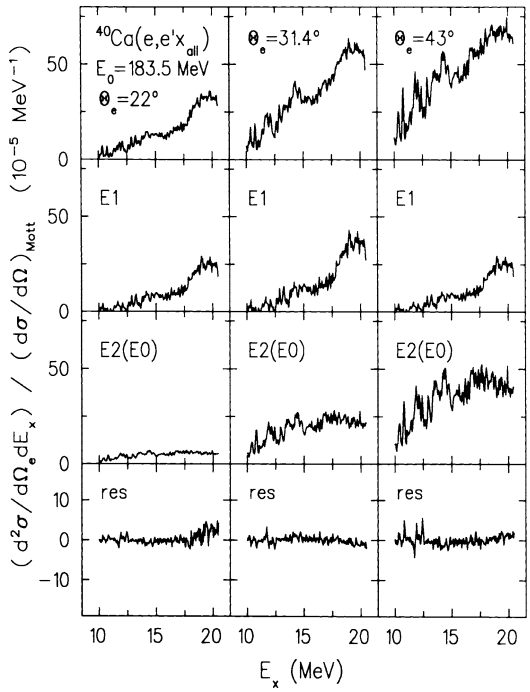

Fig. 1. The 4π-integrated cross sections of the ^{40}Ca(e, e′x) reaction (top row) and decomposition into E1 (second row) and E2(E0) parts (third row). The bottom row shows the residue resulting from a fit using Eq. (2).

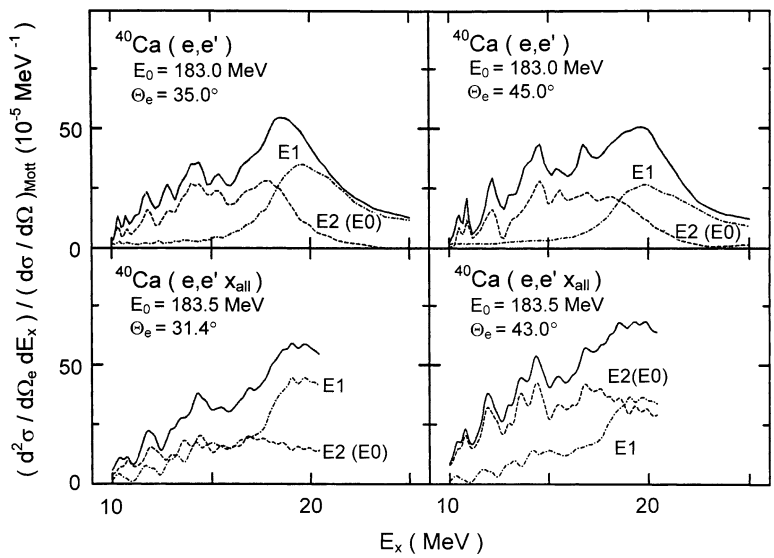

Fig. 2. Inclusive ^{40}Ca(e, e′) spectra [41] compared with 4π-integrated exclusive ^{40}Ca(e, e′x) data from the present experiment for similar kinematics. Shown are the total cross sections and their decomposition into E1 and E2(E0) parts.

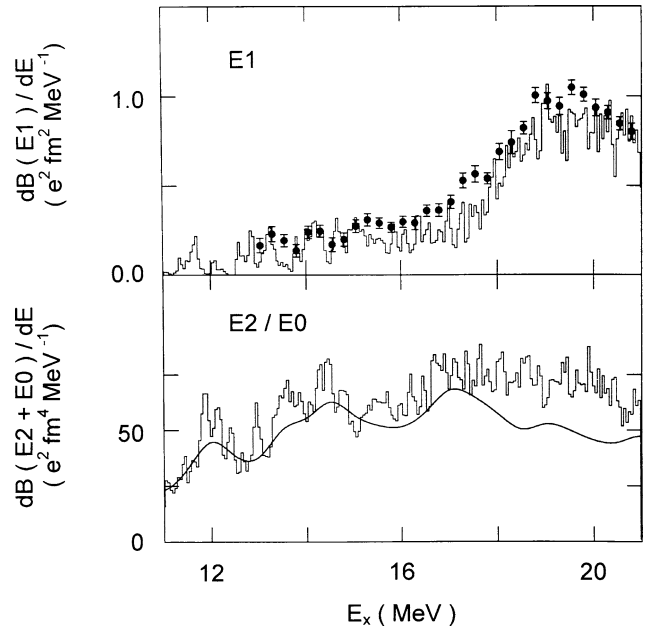

Fig. 3. Resulting B(E1) and B(E2 + E0) strength distributions in ^{40}Ca from the multipole decomposition described in Section 2.1 shown as histograms. The full circles represent $(\gamma, x;$ $x = \mathrm{p}, \alpha)$ cross sections obtained from the difference of a total photoabsorption [1] and a (γ, n) [2] experiment and converted to B(E1) strength. The solid line shows the summed B(E2) and B(E0) strengths from the calculations of [36].

circles represent the B(E1) values from the (γ, x) reaction. The agreement is very good with some minor deviations around $E_\mathrm{x} = 17$ MeV. The E2 + E0 strength with dominant structures around 12, 14 and 17 MeV is compared to a continuum RPA calculation, allowing beyond the usual 1p–1h model space also for 1p–1h $\otimes$ phonon configurations [36,37]. The latter are included because of the well-known importance of the coupling to phonons for the damping of giant resonances [42]. The solid line corresponds to the sum of E2 and E0 (appropriately weighted using the relation $B(\mathrm{E0}) = (25/16\pi) \cdot B(\mathrm{E2})$ valid at the photon point [14]) strength distributions folded with the experimental resolution $\Delta E =$ 120 keV (FWHM). The agreement is remarkably good, the main structures are reproduced over the whole excitation energy range, and also the total strength is accounted for. In contrast to all earlier 1p–1h RPA calculations, significant strength below 15 MeV excitation is predicted in this approach, in accord with experiment. This strength can be traced back to the additional g.s. correlations induced by the 1p–1h $\otimes$ phonon configurations providing yet another example of a considerable softening of the Fermi surface in ^{40}Ca with respect to the independent particle model expectations of doubly closed shells. The calculations indicate that both the GMR and the GQR are fragmented strongly over large excitation energy ranges and that the low-energy strength is shared between both, in accord with the findings of [3,7,23,24,28].

2.3. Form factor analysis

An E1 and E2(E0) multipole cross-section decomposition using the form factors of Section 2.1 is presented in Fig. 4. Overall, the experimental dependence is accounted for well except for the resulting E1 part at the lowest q (0.26 fm^{-1}) which is somewhat low, although still within error bars. The good description at the highest momentum transfers in these measurements limits possible cross-section contributions from higher multipolarites (E3) to less than 5%. In fact, the appearance of isoscalar E3 strength exhausting a significant part of the EWSR in the energy range 10–20 MeV would contradict theoretical expectations which predict low-energy strength (experimentally well established) and a high-energy resonance at about 30 MeV [43].

The form factor method can be applied also to the analysis of partial decay channels shown in Fig. 5. Appreciable differences are observed in the p decay to different final states. For example, the ratio of E1 to E2(E0) cross sections is much larger for the decay into low-lying excited states of ^{39}K (p_{123}) than for the g.s. decay or for the population of higher-lying states. Overall, the description of the experimental data is satisfactory, thereby excluding contributions of E3 strength beyond the 5% level for any of the particle decay channels analysed. Considering the substantial suppression expected due to isospin selection rules, unexpectedly large E1 cross sections are found in the α_0 decay.

The decomposed cross sections can be converted to transition strengths with the aid of the form factors displayed in Fig. 5. Table 1 summarizes the exhaustion of the E1 and E2 EWSR in the energy range 11–20.5 MeV. Note that because of the individual form factor decomposition, the EWSR exhaustions deduced for the partial channels can differ from that deduced for the total spectra (x, p, α). The E2 EWSR values are calculated assuming isoscalar excitations only. Furthermore, as pointed out above, they contain an unknown E0 part. Following theoretical predictions [36,37] one would expect an about equal share between monopole and quadrupole strength which would convert the value of 102% E2

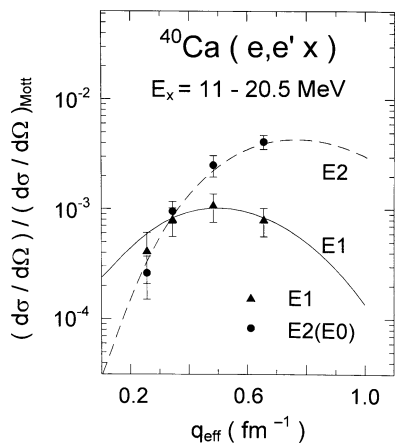

Fig. 4. Form factors of the ^{40}Ca(e, e′x) reaction summed over an interval $E_x = 11$–20.5 MeV in comparison to RPA calculations for E1 (solid line) and E2 (dashed line) transitions, see text.

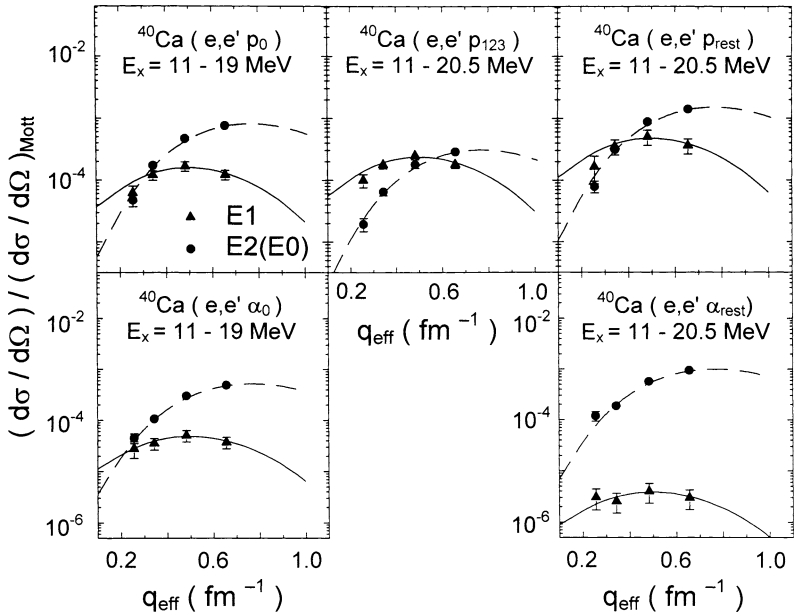

Fig. 5. Form factor decomposition of E1 and E2(E0) strength in ^{40}Ca for different decay channels. The dashed and solid lines are RPA calculations for E1 and E2 transitions, respectively (see text).

Table 1
Exhaustion of the isovector E1 and isoscalar E2 EWSR in ^{40}Ca resulting from a multipole decomposition of the (e, e′x) data and individual decay channels using RPA form factors

Channel	E1 (% EWSR)	E2 (% EWSR)
$p+\alpha$	44(19)	104(24)
p	41(15)	66(18)
p_0	7(4)	15(6)
p_{123}	10(4)	7(3)
p_{res}	34(17)	37(12)
α	<16	33(8)
α_0	<4	10(4)
α_{res}	<10	22(6)

The E2 strengths are upper limits only because the cross sections contain an unknown E0 part (see text).

EWSR given for the total (e, e′x) cross section in Table 1 to 68% of the isoscalar EWSR for both E2 and E0. When comparing the deduced values to those of other experiments it should be kept in mind that above 16 MeV excitation the neutron decay part of the cross section remains undetected although its contribution was shown to be less than 20% at the maximum of the GDR [2]. Also, the main bump of the GDR extends up to 25 MeV excitation, therefore the present experiment cannot be expected to exhaust the Thomas–Reiche–Kuhn sum rule.

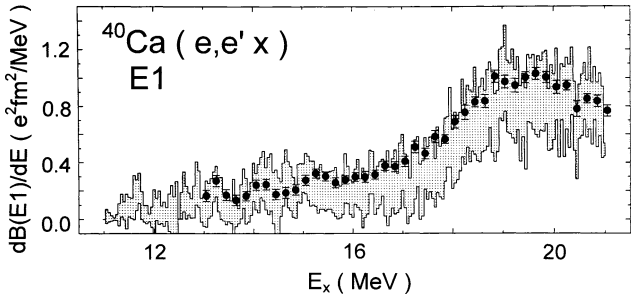

Fig. 6. The B(E1) strength distribution resulting from a multipole decomposition of the ^{40}Ca(e, e′x) data using form factors. The dashed band represents the uncertainties. The full circles are the (γ, x) data shown also in Fig. 3.

One finds that p emission for the giant resonances in ^{40}Ca dominates over α emission. Unlike in light nuclei, the decay dominantly populates higher-lying states (p_{res}). This is, however, already a strong hint for predominantly statistical proton decay (for a detailed discussion, see the following paper, part III). For the α decay channels the errors of the extrapolation of the E1 form factor to the photon point are too large to give meaningful results, so only upper limits are given. The values in Table 1 assume isovector E1 strength, i.e. excitation via the GDR and decay through $T = 0$ admixtures to the wave functions. An isoscalar character of the E1 strength can be excluded because for a squeezing mode it would show a q dependence which resembles that of E3 excitations [44]. However, recent microscopic calculations [45,46] suggest a low-lying isoscalar electric dipole mode of toroidal rather than compressional type. It would be interesting to study its form factor dependence in order to estimate the sensitivity of the present experiment to detect such a mode.

The values deduced for ^{40}Ca(e, e′x) are somewhat larger for E2(E0) and smaller for E1 than the result of the model-independent analysis [17], but still agree to within a typical systematic uncertainty of about 20%. The main difference is visualized in Fig. 6 where the B(E1) strength distribution resulting from the form factor analysis of the ^{40}Ca(e, e′x) data is shown. The shaded area corresponds to the experimental uncertainty. The full circles are again the (γ, x) data. In the model-independent method these data were used as an additional constraint to the analysis. Thus, it is not surprising that the shape of the distribution and the strength were reproduced well. The B(E1) energy distribution extracted from the form factor method is in very good agreement with the photoabsorption data. However, the resulting strength is systematically lower, though still agrees to within the error band.

3. Alpha decay angular correlations

3.1. Methods

For the description of (e, e′α) angular correlations it is useful to expand the triple-differential cross sections in terms of Legendre polynomials P_k^l:

$$\frac{\mathrm{d}^3\sigma}{\mathrm{d}\Omega_\mathrm{e}\,\mathrm{d}\Omega_\alpha\,\mathrm{d}E_\mathrm{x}} = \sigma_\mathrm{Mott}\sum_{l=0}^{2}\sum_{k=l}^{2\lambda} A_k^l P_k^l(\cos\Theta_\alpha)\cos(l\Phi_\alpha), \tag{5}$$

where λ denotes the angular momentum of the resonance. The coefficients A_k^l are determined by a fit to the data. The longitudinal and transverse response functions V_L and V_T, respectively, introduced in Eq. (1) of part I contribute to the A_k^0, while the A_k^1 coefficients give a multipole decomposition of the longitudinal-transverse interference term V_LT. The A_k^2 term, describing the expansion of the transverse-transverse interference, is removed in the present experiments by the choice of $\Phi_\alpha = 135°$. With the assumption that the resonance dominates, the Legendre polynomials can be factored into excitation form factors which are determined by the nuclear dynamics and q only, and angular correlation coefficients which depend on the particle emission and E_x, but are independent of q. Following the static-limit resonance approximation (SLRA) of [18] the Legendre coefficients can be expanded as a function of the multipole-dependent excitation form factors. The full expressions are given, e.g., in the appendix of [21].

For the kinematics of the present data measured at MAMI these relations can be simplified further by assuming that contributions due to the V_T and V_LT terms can be neglected, i.e., the excitation is purely longitudinal. For a $J^\pi = 0^+$ target and within the framework of SLRA the A_k can be expressed as

$$A_k = \sum_{\substack{\ell\ell',JJ'\\ S}} A_k'(S;\ell J;\ell' J')\left(C_{\ell J}^{(S)}\,\mathrm{e}^{\mathrm{i}\delta_{\ell J}^{(S)}}\right)^*\left(C_{\ell' J'}^{(S)}\,\mathrm{e}^{\mathrm{i}\delta_{\ell' J'}^{(S)}}\right). \tag{6}$$

The factors A_k' contain the angular momentum coupling information and are described in the appendix of [28]. The quantity $C_{\ell J}^{(S)}\,\mathrm{e}^{\mathrm{i}\delta_{\ell J}^{(S)}}$ is the complex amplitude of the product between the longitudinal matrix element and the overlap of the intermediate resonance J and the decay channel (ℓS). For $J^\pi = 0^+$ targets, the multipolarity λ of the excitation is identical to the angular momentum J of the resonance. The quantity ℓ is identified with the relative orbital angular momentum of the emitted particle with respect to the remaining nucleus, and S represents the spin of the final state determined by the coupling of the spins of the particle and of the state in the residual nucleus. The expansion parameter k can be understood as the angular momentum resulting from the coupling of two interfering resonances J and J'. Because the α particle has total angular momentum zero, the decay to the ground state of ^{36}Ar ($J^\pi = 0^+$) gives $S = 0$ whereas, the first excited state of ^{36}Ar ($J^\pi = 2^+$) yields $S = 2$.

For the particularly simple case of decay to a $J^\pi = 0^+$ final state (e.g. α_0 decay) and restriction to resonances $J \leqslant 2$ an analytical solution can be derived for the multipole decomposition of the cross sections [19]. Recently, it has been demonstrated [28] that this method can be extended to the case of emission to a $J^\pi = 2^+$ state (α_1 decay) with a few additional assumptions. With the branching of the decay of a given resonance J via different allowed angular momenta ℓ governed by the transmission coefficients and for a particular choice of phases between these ℓ-values one arrives at equations of the same structure as those for the α_0 case (see the appendix in [28]).

3.2. Results

The analysis of the ^{40}Ca(e, e′α_0) and ^{40}Ca(e, e′α_1) angular correlations and the physics implications of the resulting E0 and E2 strength distributions have been discussed in detail in [23,28] and here these results will not be dwelt upon further. Rather, a few additional subjects not covered in [23,28] will be discussed.

The assumption of purely longitudinal cross sections, while representing a good assumption for the data analyzed in [23,28], is not justified for the kinematics of the measurement at the S-DALINAC. It is, therefore, of interest to test the application of the methods described in Section 3.1 to a more general case where V_{T} and V_{LT} terms are included. The transverse matrix elements cannot be determined in a unique way from a fit to the data. Thus, Siegert's theorem

$$\frac{TJ}{LJ} = -\frac{E_{\mathrm{x}}}{q\hbar c}\sqrt{\frac{J+1}{J}} \tag{7}$$

relating the transverse (TJ) and longitudinal (LJ) matrix elements is used to constrain the degrees of freedom.

Fig. 7 displays the angular correlations of the α_0 decay following electro-excitation of ^{40}Ca measured at $E_0 = 78$ MeV and $\Theta_{\mathrm{e}} = 40°$. The solid lines are fits using Eqs. (5) and (7), accounting for the data quite well. The need for a transverse cross-section contribution is visible in a shift of the first maximum from $\Theta_\alpha = 0°$ expected for purely longitudinal excitations to about 10°. This shift is caused by the LT interference term which is expressed in the expansion discussed in Section 3.1 through an associated Legendre polynomial A_k^1. The cross-section decomposition shows a dominance of E0 and E2 multipoles, but E1 contributions no longer are negligible because of an enhancement due to the low momentum transfer.

The resulting E0 and E2 cross-section distributions are displayed in Fig. 8 together with the results obtained from an analysis of the ^{40}Ca(e, e′α_0) data measured at higher electron energies [23] and ^{40}Ca(α, $\alpha'\alpha_0$) data measured in kinematics where either E0 [24] or E2 [3] dominate. The agreement between the two independent analyses from electron scattering is quite good. Remaining small differences might originate from the somewhat limited statistics of the low incident-energy data and the additional assumptions made about the transverse cross-section part. With respect to the α-induced data one finds good correspondence between the main structures in the E2 distributions (note, however, the discrepancies of the EWSR exhaustion [23,25]). The E0 cross sections from the (α, $\alpha'\alpha_0$) experiment are somewhat hampered by poor statistics. Prominent structures are seen around 14 and 16–17 MeV excitation, in accordance with the electron scattering results. At lower excitation energy the differences are larger. It should be noted that the agreement is better for inclusive (α, α') spectra from the same experiments [24] measured at 0° where E0 excitations dominate the cross sections.

An interesting difference is observed in the momentum transfer dependence of the α_0 decay following electro-excitation of the GMR and GQR. This is demonstrated in Fig. 9, where the corresponding form factors summed over excitation energy are shown. The

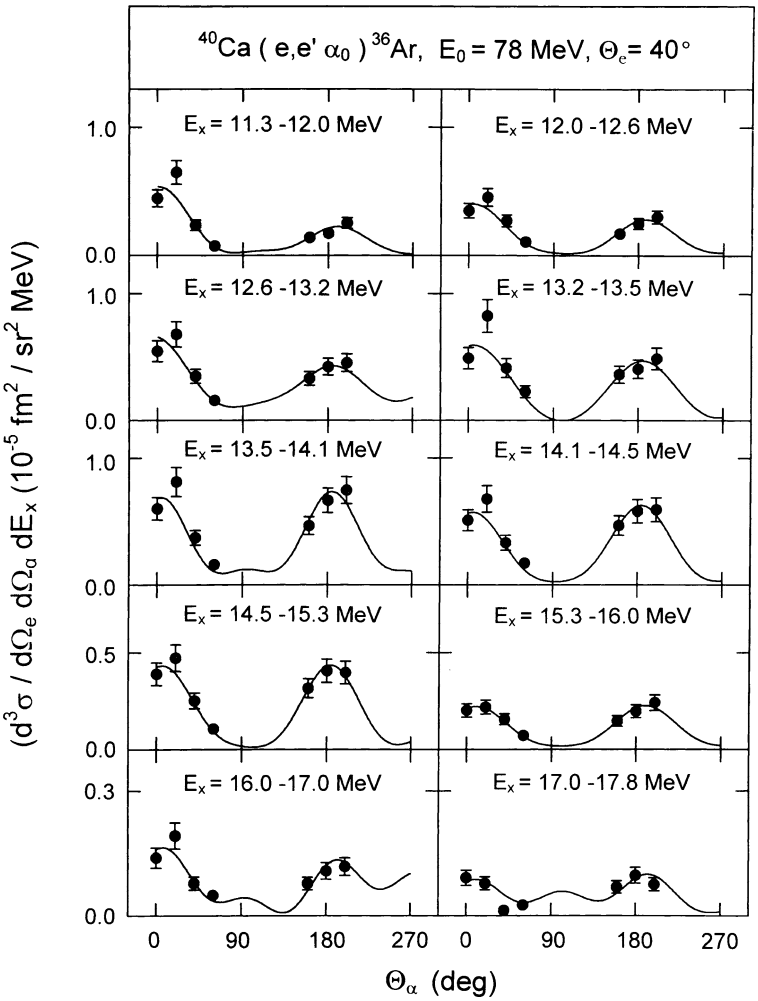

Fig. 7. Angular correlations of the ^{40}Ca(e, e′α_0) reaction measured at $E_0 = 78$ MeV and $\Theta_e = 40°$ for different excitation energy bins. The solid lines are fits with the angular correlation function (5) as described in the text.

variation as a function of the effective momentum transfer is expected to be the same at low q_{eff} which also results from the microscopic form factor calculations discussed in Section 2. By way of example, the results of [34] for E0 and E2 strenghts are displayed in Fig. 9. The experimentally derived E2 form factor follows closely the microscopic prediction. However, the E0 form factor shows a marked enhancement over the calculations increasing towards lower momentum transfers. At present, this behaviour is theoretically not understood. On the other hand, if this different form factor behaviour of E0 and E2 strength could be established as a general phenomenon, it would offer a new path to an experimental separation of GMR and GQR contributions which overlap strongly in medium-mass nuclei.

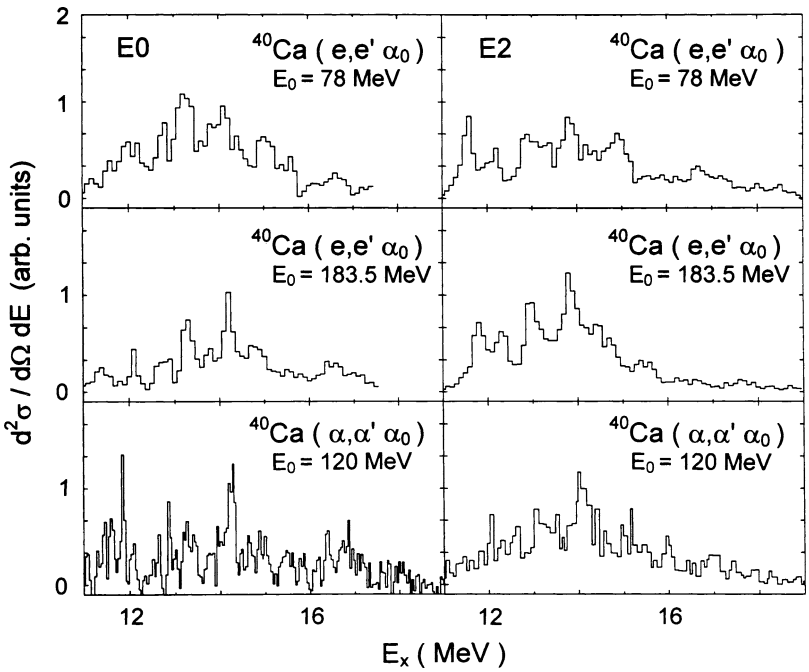

Fig. 8. Comparison of E0 and E2 cross-section distributions in ^{40}Ca coincident with α_0 decay obtained from (e, e′α_0) at $E_0 = 78$ MeV, (e, e′α_0) at $E_0 = 183.5$ MeV and (α, $\alpha'\alpha_0$) reactions [3,24].

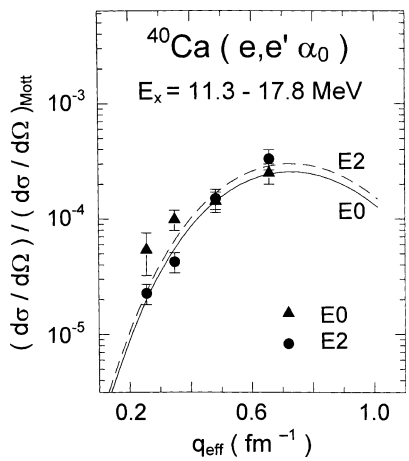

Fig. 9. Form factors of the decomposed E0 and E2 parts in the ^{40}Ca(e, e′α_0) reaction. The solid and dashed lines are the microscopic predictions of [34].

4. Proton decay angular correlations

4.1. Shell model and continuum RPA description

Compared to the $(e, e'\alpha)$ case discussed in the previous section the analysis of $(e, e'p)$ angular correlations is considerably more complex. The number of partial decay angular momenta can become quite large, depending on the final state spin. An additional complication are the 'channel spins' resulting from the coupling of the proton intrinsic spin to the orbital angular momentum requiring the corresponding individual ACFs to be added incoherently.

Due to this complexity it is not possible to derive useful information on the multipole composition from the coefficients of a Legendre polynomial fit to the data in cases where several multipoles contribute with comparable cross sections. Thus, a model description of the $(e, e'p)$ ACFs is needed. In the course of this work two approaches were tested, a shell-model description in the SLRA framework [18] assuming direct knockout of a nucleon, and a self-consistent continuum RPA calculation [32].

The shell-model calculations were performed with the code NEWTON [47]. It has been applied quite successfully to the description of the $^{12}C(e, e'p)$ reaction [29]. The calculations are limited to longitudinal excitations (sufficient for the higher q measured at Mainz) treated in PWBA which is a reasonable approximation in light nuclei, but might be questionable already in the case of ^{40}Ca. A direct nucleon knockout was assumed for the decay, and the excited state wave functions were determined with the optical model parameters of [48].

The approach was tested for two particularly simple cases where a single multipolarity is known to dominate: the $E_x = 13.7$–15.0 MeV region for $q = 0.49$ fm^{-1} (E2), and the $E_x = 19.0$–20.0 MeV region for $q = 0.35$ fm^{-1} (E1). With the mixing coefficients and phases fixed from these data sets it was tried in the next step to obtain the ACFs for the other momentum transfers. This turned out to be impossible. Furthermore, an extreme sensitivity of the results to small variations of the optical model parameters was observed. We concluded that probably the underlying picture of a simple one-step knockout process is too simple.

An alternative is presented by a continuum RPA model for photon- and electron-induced nucleon emission [32] which has been tested successfully in the quasielastic regime [49] and in the interference region between dominance of resonance and quasi-elastic strengths [33]. Although developed initially for quasielastic reactions a motivation for its application was the finding in the present results of predominant semidirect decay to the low-lying states in ^{39}K. This is discussed in detail in the subsequent paper (part III).

In this model [32] the initial and final state wave-functions are calculated with the Hartree–Fock (HF) method. The HF potential is determined by a Skyrme force which has been modified to include a radius-dependent three-body term (Ske2 in [50]). The parameters have been fixed by a comparison with numerous data sets and have been shown to give good results for g.s. binding energies and nuclear radii over a wide mass range [50]. Excitation of multipole strengths is calculated in 1p–1h RPA. The residual interaction is

derived from the above described Skyrme force also. Thus, the present approach allows for a self-consistent treatment of the g.s. and the excited states. Electro-excitation of natural-parity multipoles $\lambda = 1$–5 was taken into account. The electron wave functions were calculated in PWBA. Coulomb distortion effects were partly corrected for by the introduction of an effective momentum transfer (see Section 2).

A clear advantage of the RPA treatment over the shell-model approach is that certain classes of multistep processes are allowed, i.e. scattering and reabsorption of the nucleon in the nuclear medium. It will be demonstrated below that the inclusion of the RPA correlations is essential in order to achieve a good description of the angular correlations.

4.2. Results

As discussed in part I, measured angular correlations could be extracted for the p_0–p_3 channels. The following discussion is restricted to the decay to the ^{39}K g.s. (p_0) and first excited state (p_1) which show, respectively, a dominant $1d_{3/2}$ and $2s_{1/2}$ single-hole structure with respect to ^{40}Ca. Figs. 10 and 11 present angular correlations measured at

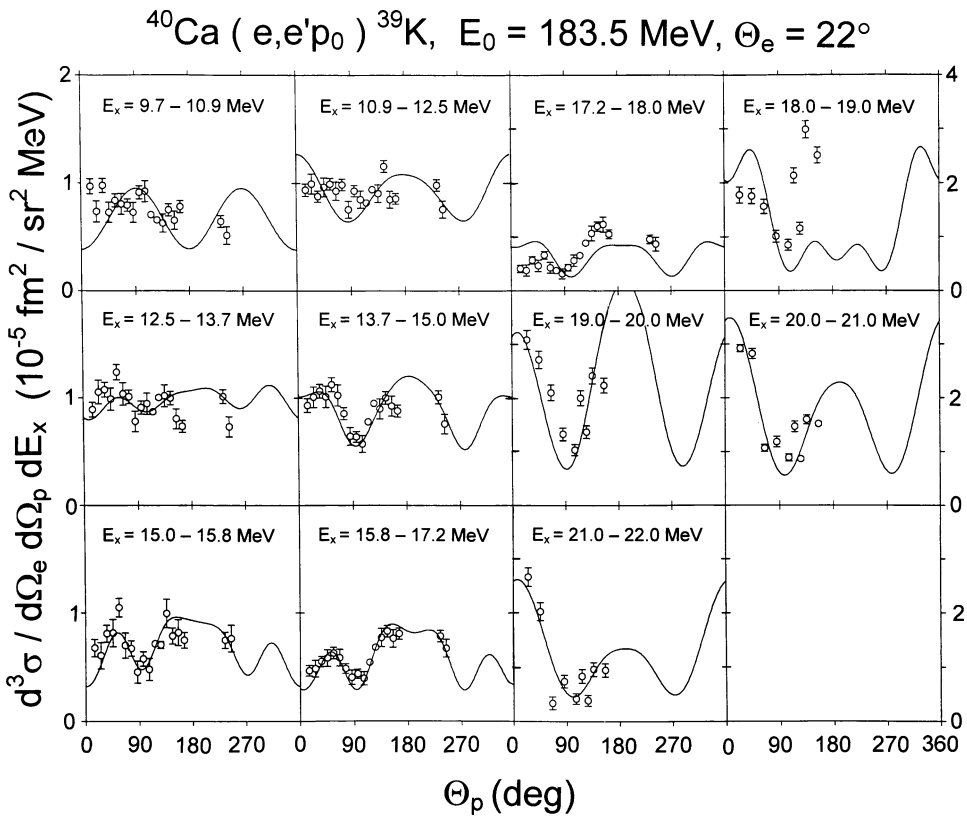

Fig. 10. Angular correlations of the ^{40}Ca(e, e′p$_0$) reaction measured at $E_0 = 183.5$ MeV and $\Theta_e = 22°$ for different excitation energy bins. The solid lines represent calculations with the continuum-RPA model of [32] normalized to the data.

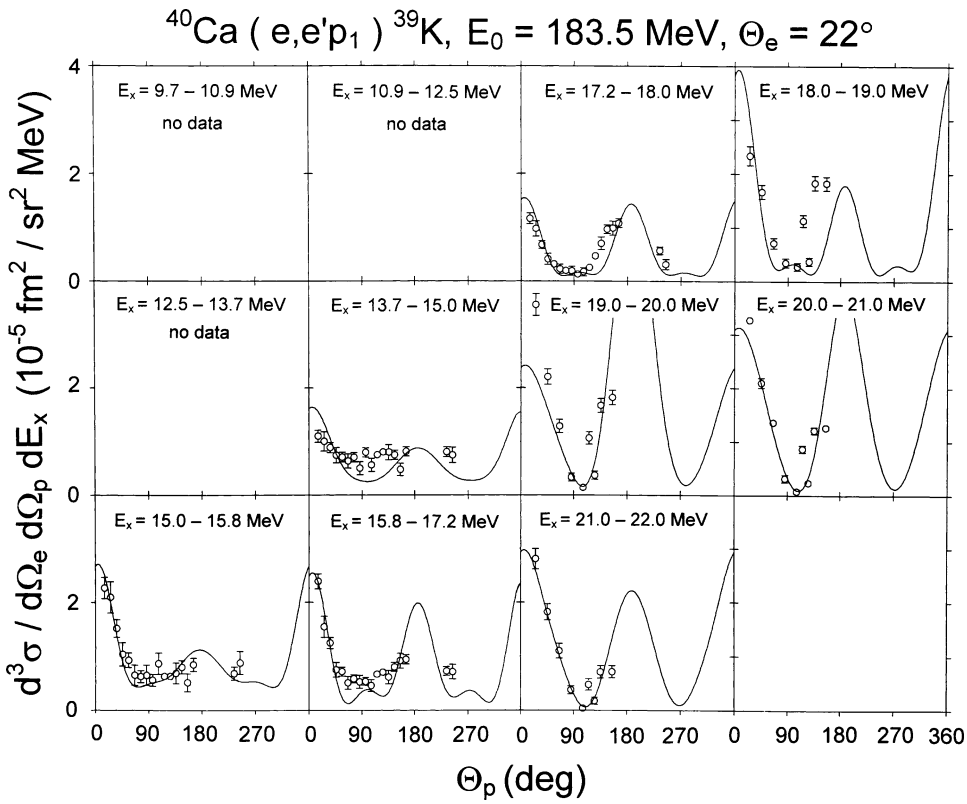

Fig. 11. Angular correlations of the ^{40}Ca(e, e′p$_1$) reaction measured at $E_0 = 183.5$ MeV and $\Theta_e = 22°$ for different excitation energy bins. The solid lines represent calculations with the continuum-RPA model of [32] normalized to the data.

$E_0 = 183.5$ MeV, $\Theta_e = 22°$ for an excitation energy range $E_x = 9.7$–22.0 MeV and with energy bins of about 1 MeV width. The choice of these bins was on one hand limited by the need of sufficient statistics and on the other hand followed the observation of prominent gross structures in the (e, e′p) excitation spectrum (see part I). The calculated ACFs were normalized to the data for each energy bin.

As can be seen, there are large variations of the shapes of experimental angular correlations. Over wide excitation ranges a pronounced minimum around $\Theta_p = 90°$ is found for p_0 and p_1 decay. At excitation energies below the centroid of the GDR maxima are observed in p_0 decay around 45° and 135°, while p_1 decay shows peaking around 0° and 180°. Above 18 MeV, the angular correlations exhibit dominant $L = 1$ character, especially pronounced for the p_1 channel. This can be understood as a signature of the GDR dominance in this energy range. Similar to the α_0 decay discussed above, for decay into a $J^\pi = 1/2^+$ final state, the orbital decay angular momentum again is equal to the angular momentum of the excited multipole. The RPA results are capable of describing the data surprisingly well over the entire energy range for both decay channels. Deviations are visible around $E_x = 18$ MeV where the RPA calculation predicts the maximum of

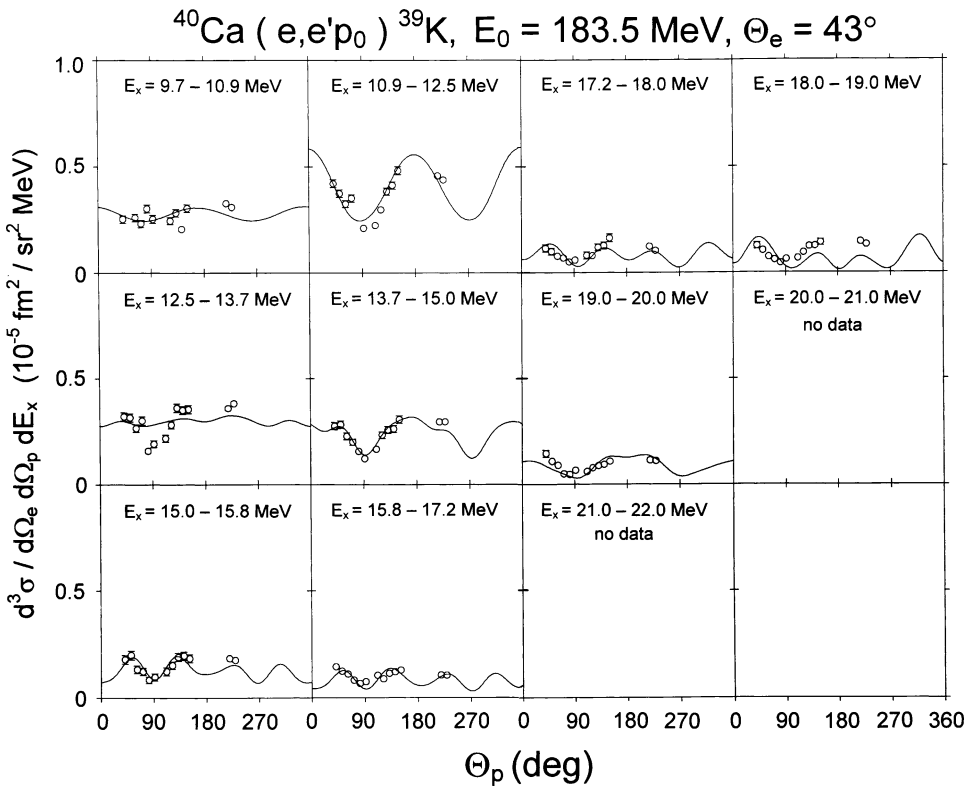

Fig. 12. Angular correlations of the ^{40}Ca(e, e′p$_0$) reaction measured at $E_0 = 183.5$ MeV and $\Theta_e = 43°$ for different excitation energy bins. The solid lines represent calculations with the continuum-RPA model of [32] normalized to the data.

the E2 and E0 resonances while the experiment finds very fragmented strengths almost equally distributed in energy (see Section 2). Otherwise, even angular correlations differing strongly from energy bin to energy bin can be accounted for. It is also noteworthy that the experimentally deduced p_0 to p_1 branching ratio is reproduced very well.

In order to study the role of the momentum transfer dependence, Fig. 12 depicts angular correlations of the ^{40}Ca(e, e′p$_0$) reaction for the highest q measurement ($E_0 = 183.5$ MeV, $\Theta_e = 43°$). The global structures in the experimental angular correlations persist for all momentum transfers, although some variations in detail are visible (see, e.g., the $E_x =$ 10.9–12.5 MeV interval in both data sets). The description achieved by the continuum RPA approach remains of comparable quality. This is indeed true also for all the other (e, e′p) angular correlation results not shown here (for a full account of the results see [51]).

It is interesting to extend the present analysis to a case where the assumption of purely longitudinal electron scattering cross sections no longer holds. Such a case is given for the kinematics of the lowest measured q-point ($E_0 = 78$ MeV, $\Theta_e = 40°$) as discussed in Section 3. Transverse and longitudinal-transverse contributions to the coincidence cross sections are taken into account in the calculations. Fig. 13 shows results for the ^{40}Ca(e, e′p$_{123}$)

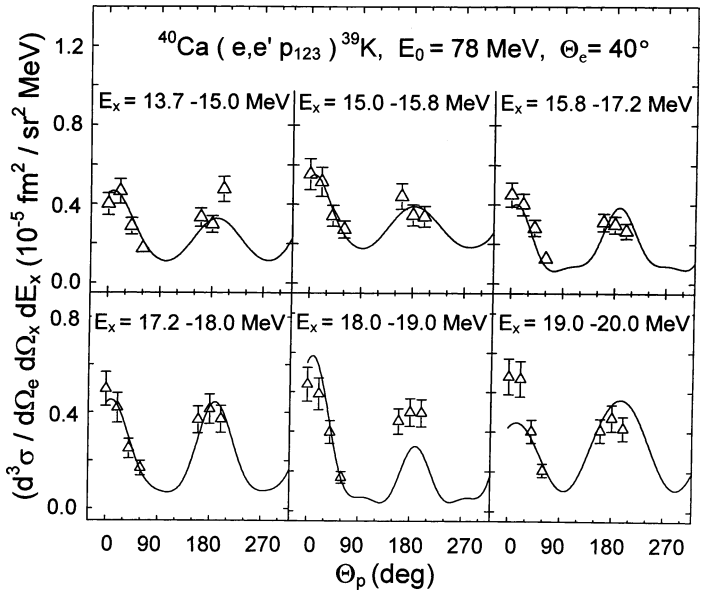

Fig. 13. Angular correlations of the ^{40}Ca(e, e′p$_{123}$) reaction measured at $E_0 = 78$ MeV and $\Theta_e = 40°$ for different excitation energy bins. The solid lines represent calculations with the continuum-RPA model of [32] normalized to the data.

reaction (because of limited statistics the sum of p_1, p_2 and p_3 is taken). It is interesting to note that despite the summation over various final states the ACF still keep pronounced structures of a forward–backward asymmetry. Again, the data can be described rather well.

The success of the calculations comes somewhat as a surprise because — as discussed above — the calculation of the initial strength distributions based on RPA only cannot provide a satisfactory description of the GQR and GMR. This is reflected in strongly energy-dependent factors for the overall normalization to the experimental angular correlations. Deviations from the experimental results are visible in Figs. 10–12 around 18 MeV excitation where the RPA predicts the main concentration of the GQR to be, in contrast to the experimental results. The overall very good description of the (e, e′p) angular correlations indicates that its properties are more sensitive to the final state interaction. A detailed analysis reveals that these are dominated by charge-exchange rescattering processes of the type (e, e′n)(n, p) while direct knock-out contributions play a minor role [17,52].

This is demonstrated in the upper part of Fig. 14 for the example of the $E_x = 18$–19 MeV energy bin measured at $q = 0.49$ fm^{-1}. The direct knock-out part (shown as dashed line) cannot explain the experimentally observed angular correlations. The argument is aggravated further by comparison to the ^{40}Ca(e, e′n$_0$) angular correlation for the same excitation energy bin and similar momentum transfer taken from [31] displayed in the lower part of Fig. 14. Again, the full result gives very good agreement while a pure knock-out calculation cannot account for the data. Furthermore, pure neutron knock-out from ^{40}Ca is predicted to be negligible compared to the total cross section.

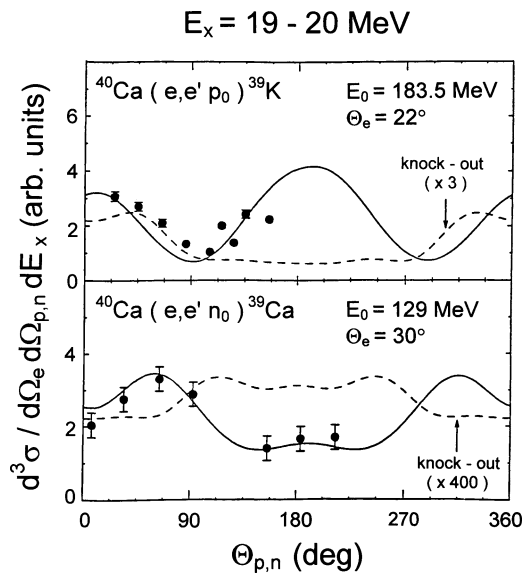

Fig. 14. Comparison of the angular correlations for 19–20 MeV excitation energy in the ^{40}Ca(e, e′p$_0$) (present work) and ^{40}Ca(e, e′n$_0$) [31] reactions at similar momentum transfer. The solid lines are the full continuum-RPA calculations of [32] normalized to the data while the dashed lines represent the direct knockout cross-section contributions only.

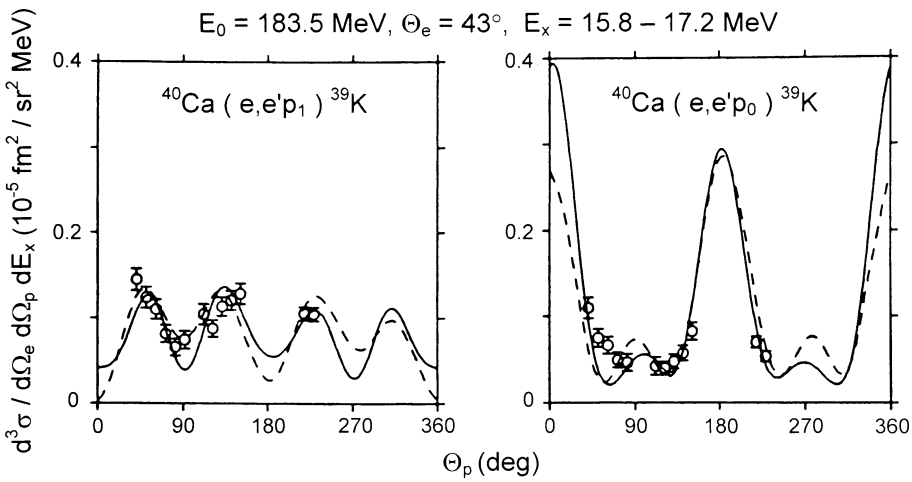

Fig. 15. Angular correlations of the ^{40}Ca(e, e′p$_0$) and (e, e′p$_1$) reactions measured at $E_0 = 183.5$ MeV and $\Theta_e = 43°$ for an excitation energy bin 15.8–17.2 MeV. The solid and dashed lines represent continuum-RPA model calculations of [32] and [53], respectively, normalized to the data.

Finally, another continuum RPA calculation [53] is touched upon briefly which allows comparison for selected data at the kinematics of the highest momentum transfer (Fig. 15). The calculations were performed at the maximum of the theoretical E2 strength distribution which coincides with one of the peaks of E2(E0) strength deduced from the multipole

decomposition in Section 2. In this work, the single-particle properties were obtained from a Woods–Saxon potential and an effective residual interaction of the Landau–Migdal type was used. The ACFs thus determined for both the p_0 and p_1 decays are depicted in Fig. 15 as dashed lines while the results using the model of [32] are plotted as solid lines. Both calculations give rather similar results with only small differences for the depth of the minima around 90° and 180° for the $(e, e'p_0)$ case and slight shift of the maximum around 90° in the $(e, e'p_1)$ channel. The mutual success of both approaches indicates that, while the total E2 strength at this excitation energy certainly is overestimated because of the limitation of both calculations to the 1p–1h level, at least the microscopic structure seems to be accounted for well.

5. Conclusions

The present paper discussed various methods of decomposing the contributions of the overlapping GMR, GDR and GQR in ^{40}Ca using coincident electron scattering data.

One possibility has been to utilize the form factor dependence of the different multipoles for the 4π-integrated cross sections. Two different approaches were presented here, one so-called 'model-independent' (which is in fact not unique, but needs additional constraints such as $^{40}\mathrm{Ca}(\gamma, x)$ cross sections also to be used) and one using form factors calculated microscopically as input. Both methods agree generally within a systematic uncertainty of about 20%. The resulting B(E1) strength distribution and the exhaustion of the GDR EWSR in the excitation energy region investigated agrees well with photoabsorption data. The E0 and E2 contributions cannot be separated because the form factors are expected to be very similar. The summed B(E0) and B(E2) strength distribution is highly fragmented and extends to low excitation energies of about 12 MeV. These properties of the GMR and GQR can be explained quite accurately within a microscopic continuum RPA calculation which includes, beyond the usual 1p–1h space, coupling to the low-lying surface vibrations and the g.s. correlations induced by these additional configurations. The latter are found to be responsible for the appearance of sizable strength below $E_x = 15$ MeV.

A powerful tool allowing for the complete decomposition of E0, E1 and E2 cross sections are $(e, e'\alpha)$ angular correlations. The results for ^{40}Ca have been discussed in detail elsewhere [23,28] and only a few special aspects are presented here. It is investigated whether the decomposition methods developed for purely longitudinal cross sections can be extended to cases where transverse parts are nonnegligible. The results show that this is indeed possible, assuming Siegert's theorem to hold, in accordance with findings in investigations of the $(e, e'\alpha_0)$ reactions in ^{12}C and ^{16}O (the latter cases, however, were simplified by the dominance of one multipole). The experimental form factors of the cumulated E0 and E2 strengths in the $^{40}\mathrm{Ca}(e, e'\alpha_0)$ reaction exhibit a surprisingly different behaviour at low momentum transfer. The q dependence, which should be the same, is indeed similar near the maxima of the E0 and E2 form factors. However, contrary to expectations the differences increase towards lower momentum transfer. At present there is no explanation for such a result. If this difference could be shown to be a general

phenomenon it would open up a new way to achieve E0/E2 separation in electron scattering not limited to particular decay channels.

Proton decay angular-correlations are more complicated because of the large number of partial decay angular momenta and the occurrence of channel spin. This precludes an extraction of multipole strength amplitudes from the Legendre polynomial fits except for the simplest cases. Here, the ^{40}Ca(e, e′p) angular correlations populating low-lying states in ^{39}K were compared with a self-consistent continuum-RPA approach using a Skyrme force. The strong variations of the angular correlation shapes as a function of excitation energy and momentum transfer is accounted for impressively. This is somewhat surprising since the multipole strengths are calculated in 1p–1h RPA only which clearly does not account for the complex GMR and GQR distributions. Rather, the calculations imply that final state interactions largely determine the angle dependence of the nucleon decay from the giant resonance region in ^{40}Ca. Specifically, the calculations predict charge exchange reactions of the type (e, e′n)(n, p) to dominate. These results demonstrate also that a pure knockout picture of the (e, e′p) reactions is far too simple.

To summarize, the examples presented here demonstrate the power of electro-induced coincidence studies for detailed investigations of the structure of giant resonances. The wealth of spectroscopic information allows stringent tests of our present understanding of the nuclear response in ^{40}Ca for multipoles of low angular momentum.

Acknowledgements

We thank M.N. Harakeh, S. Kamerdzhiev, J. Speth, A. van der Woude, G.J. Wagner, J. Wambach and D.H. Youngblood for useful discussions.

References

[1] J. Ahrens, H. Borchert, K.H. Czock, H.B. Eppler, H. Gimm, H. Gundrum, M. Kröning, P. Riehn, G. Sita Ram, A. Ziegler, B. Ziegler, Nucl. Phys. A 251 (1975) 479.
[2] D. Brajnik, D. Jamnik, G. Kernel, U. Miklavzic, A. Stanovnik, Phys. Rev. C 9 (1974) 1901.
[3] F. Zwarts, A.G. Drentje, M.N. Harakeh, A. van der Woude, Phys. Lett. B 125 (1983) 123; F. Zwarts, A.G. Drentje, M.N. Harakeh, A. van der Woude, Nucl. Phys. A 439 (1985) 117.
[4] T. Hoshimo, A. Arima, Phys. Rev. Lett. 37 (1976) 266.
[5] P.F. Bortignon, R.A. Broglia, Nucl. Phys. A 371 (1981) 405.
[6] S. Drożdż, V. Klemt, J. Speth, J. Wambach, Nucl. Phys. A 451 (1986) 11.
[7] D.H. Youngblood, H.L. Clark, Y.-W. Lui, Phys. Rev. C 55 (1997) 2811.
[8] G. Kühner, D. Meuer, S. Müller, A. Richter, E. Spamer, O. Titze, W. Knüpfer, Phys. Lett. B 104 (1981) 189.
[9] S. Kamerdzhiev, J. Lisantti, P. von Neumann-Cosel, A. Richter, G. Tertychny, J. Wambach, Phys. Rev. C 55 (1997) 2101.
[10] D. Lacroix, A. Mai, P. von Neumann-Cosel, A. Richter, J. Wambach, Phys. Lett. B 479 (2000) 15.
[11] J. Heisenberg, H.P. Blok, Annu. Rev. Nucl. Part. Sci. 33 (1983) 569.
[12] T. Kihm, K.T. Knöpfle, H. Riedesel, P. Voruganti, H.J. Emrich, G. Fricke, R. Neuhausen, R.K.M. Schneider, Phys. Rev. Lett. 56 (1986) 2789.

[13] T. Weber, R.D. Heil, U. Kneissl, W. Pecno, W. Wilke, H.J. Emrich, T. Kihm, K.T. Knöpfle, Phys. Rev. Lett. 59 (1987) 2028.
[14] G.O. Bolme, L.S. Cardman, R. Doerfler, L.J. Koester Jr., B.L. Miller, C.N. Papanicolas, H. Rothhaas, S.E. Williamson, Phys. Rev. Lett. 61 (1988) 1081.
[15] R.A. Miskimen, E.A. Ammons, J.D.T. Arruda-Neto, L.S. Cardman, P.L. Cole, J.R. Deininger, S.M. Dolfini, A.J. Linzey, J.B. Mandeville, B.L. Miller, P.E. Mueller, C.N. Papanicolas, A. Serdarevič, S.E. Williamson, Phys. Lett. B 236 (1990) 251;
R.A. Miskimen, E.A. Ammons, J.D.T. Arruda-Neto, G.O. Bolme, L.S. Cardman, P.L. Cole, J.R. Deininger, S.M. Dolfini, A.J. Linzey, J.B. Mandeville, B.L. Miller, P.E. Mueller, C.N. Papanicolas, A. Serdarevič, S.E. Williamson, Phys. Rev. C 43 (1991) 1677.
[16] S. Strauch, P. von Neumann-Cosel, C. Rangacharyulu, A. Richter, G. Schrieder, K. Schweda, J. Wambach, Phys. Rev. Lett. 85 (2000) 2913.
[17] H. Diesener, U. Helm, G. Herbert, V. Huck, P. von Neumann-Cosel, C. Rangacharyulu, A. Richter, G. Schrieder, A. Stascheck, A. Stiller, R. Ryckebusch, J. Carter, Phys. Rev. Lett. 72 (1994) 1994.
[18] W.E. Kleppinger, J.D. Walecka, Ann. Phys. (NY) 146 (1983) 349.
[19] M. Spahn, T. Kihm, K.T. Knöpfle, Z. Phys. A 330 (1988) 345.
[20] J.P. Fritsch, H.J. Emrich, A. Grasmück, R. Neuhausen, S. Schardt, N. Zimmermann, J.R. Calarco, M. Potokar, Phys. Rev. Lett. 68 (1992) 1667.
[21] J. DeAngelis, J.R. Calarco, J.E. Wise, H.J. Emrich, R. Neuhausen, H. Weyand, Phys. Rev. Lett. 70 (1993) 2872;
J. DeAngelis, J.R. Calarco, J.E. Wise, H.J. Emrich, R. Neuhausen, H. Weyand, Phys. Rev. C 52 (1995) 61.
[22] L.A.A. Terremeto, V.P. Likachev, M.N. Martins, H.J. Emrich, G. Fricke, T. Kröhl, K.W. Neff, Phys. Rev. C 56 (1997) 2597.
[23] H. Diesener, U. Helm, P. von Neumann-Cosel, A. Richter, G. Schrieder, S. Strauch, Phys. Lett. B 352 (1995) 201.
[24] S. Brandenburg, R. De Leo, A.G. Drentje, M.N. Harakeh, H. Sakai, A. van der Woude, Phys. Lett. B 130 (1983) 9.
[25] J. Carter, A.A. Cowley, H. Diesener, R.W. Fearick, S.V. Förtsch, M.N. Harakeh, J.J. Lawrie, S.J. Mills, P. von Neumann-Cosel, R.T. Newman, J.V. Pilcher, A. Richter, K. Schweda, F.D. Smit, G.F. Steyn, S. Strauch, D.M. Whittal, Nucl. Phys. A 630 (1998) 631.
[26] K. Schweda, J. Carter, H. Diesener, R.W. Fearick, S.V. Förtsch, J.J. Lawrie, P. von Neumann-Cosel, R.T. Newman, J.V. Pilcher, A. Richter, F.D. Smit, G.F. Steyn, S. Strauch, Phys. Lett. B 506 (2001) 247.
[27] J. Carter, H. Diesener, R.W. Fearick, S.V. Förtsch, J.J. Lawrie, P. von Neumann-Cosel, R.T. Newman, J.V. Pilcher, A. Richter, K. Schweda, F.D. Smit, G.F. Steyn, S. Strauch, Phys. Rev. C 63 (2001) 057602.
[28] M. Kohl, P. von Neumann-Cosel, A. Richter, G. Schrieder, S. Strauch, Phys. Rev. C 57 (1998) 3167.
[29] J.R. Calarco, J. Arruda-Neto, K.A. Griffioen, S.S. Hanna, D.H.H. Hoffmann, B. Neyer, R.E. Rand, K. Wienhard, M.R. Yearian, Phys. Lett. B 146 (1984) 179;
J.R. Calarco, Nucl. Phys. A 569 (1994) 363c.
[30] A. Tanaka, T. Hino, H. Kawahara, N. Nomura, T. Tamae, M. Sugawara, H. Tsubota, H. Miyase, Y. Kawazoe, Nucl. Phys. A 489 (1988) 381.
[31] C. Takakuwa, T. Saito, S. Suzuki, K. Takahisa, T. Tohei, T. Nakagawa, A. Abe, Phys. Rev. C 50 (1994) 845.
[32] J. Ryckebusch, K. Heyde, D. Van Neck, M. Waroquier, Nucl. Phys. A 503 (1989) 694.
[33] K. Reiner, P. Grabmayr, G. Mauser, G. Mertens, G.J. Wagner, J. Friedrich, N. Voegler, K.T. Knöpfle, J. Ryckebusch, K. Heyde, D. Van Neck, M. Waroquier, Phys. Lett. B 228 (1989) 31;

J. Ryckebusch, K. Heyde, D. Van Neck, M. Waroquier, K. Reiner, P. Grabmayr, G.J. Wagner, Nucl. Phys. A 505 (1989) 755.
[34] W. Knüpfer, private communication.
[35] W. Knüpfer, M. Huber, Phys. Rev. C 14 (1976) 2254.
[36] S. Kamerdzhiev, J. Speth, G. Tertychny, Phys. Rev. Lett. 74 (1995) 3943.
[37] S. Kamerdzhiev, J. Speth, G. Tertychny, Nucl. Phys. A 624 (1997) 328.
[38] A.B. Migdal, Theory of Finite Fermi Systems and Applications to Atomic Nuclei, Wiley, New York, 1967.
[39] S. Kamerdzhiev, J. Speth, G. Tertychny, KFA Jülich Report KFA-IKP(TH)-1994-23.
[40] Th. Walcher, Prog. Part. Nucl. Phys. 34 (1995) 1.
[41] Y. Torizuka, K. Itoh, Y.M. Shin, Y. Kawazoe, H. Matsuzaki, G. Takeda, Phys. Rev. C 11 (1975) 1174.
[42] G.F. Bertsch, P.F. Bortignon, R.A. Broglia, Rev. Mod. Phys. 55 (1983) 287.
[43] A. van der Woude, Prog. Part. Nucl. Phys. 18 (1987) 217.
[44] M.N. Harakeh, A.E.L. Dieperink, Phys. Rev. C 23 (1981) 2329.
[45] G. Colò, N. Van Giai, P.F. Bortignon, M.R. Quaglia, Phys. Lett. B 485 (2000) 362.
[46] D. Vretenar, A. Wandelt, P. Ring, Phys. Lett. B 487 (2000) 334.
[47] W. Kleppinger, private communication.
[48] L.R.B. Elton, R. Swift, Nucl. Phys. A 94 (1967) 52.
[49] C. Van den Abeele, D. Ryckbosch, J. Ryckebusch, J. Dias, L. Van Hoorebecke, R. Van de Vyver, J.-O. Adler, B.-E. Andersson, L. Isaksson, H. Ruijter, B. Schröder, Phys. Lett. B 296 (1992) 302.
[50] M. Waroquier, J. Ryckebusch, J. Moreau, K. Heyde, N. Blasi, Y. van der Werf, G. Wenes, Phys. Rep. 148 (1987) 249.
[51] V. Huck, Dissertation D17, Technische Hochschule Darmstadt, 1991.
[52] P. von Neumann-Cosel, Prog. Nucl. Part. Phys. 35 (1995) 295.
[53] G. Co', A.M. Lallena, T.W. Donnelly, Nucl. Phys. A 469 (1987) 684.